

# Isoparametric Finite Element Method (FEM) Using 2D Quadrilateral Elements In the Linear Elastic Regime

(Ben Gosling - U1706745)

Using finite element techniques to understand how a material will deform under an external load is essential when designing a solid structure. This paper discusses implementing isoparametric quadrilateral elements to computationally model how a C-shaped solid structure deforms when the two ends are fixed at the x-axis, and an external load is applied at the uppermost edge. Resolutions of the solid structure varied from  $2^3 - 2^{15}$  elements, in which the deformed nodal displacements of the finite element approach implemented achieved  $< 4\%$  error for  $10^3$  elements, which further reduced to  $< 1\%$  and  $< 0.5\%$ , for system sizes  $4\times$  and  $8\times$  larger respectively. Stress and strain fields were deduced to be maximal at the vertices of coordinates (2, 2) and (6,2), corresponding to the inside corners of the fixed C-shape structure, where the strain and stress were highly concentrated around these vertices. Empirical relations of the discretisation error and the area of the finite elements are found using Bayesian regression fitting, in which error is found to fit a degree 3 polynomial with the area size. Convergence of key properties such as stress, strain and nodal displacements were observed for increasing grid resolution; however, more accurate results would be achieved by extending the model further to use a larger resolution reference solution to benchmark errors against and using higher-order shape functions and element schemes.

## I. INTRODUCTION

The finite element method is one of the most popular techniques to solve differential equations describing engineering problems such as heat transfer, fluid flow, and structural analysis discussed below in the context of this paper [1][2].

The strong form of the force balance equation is given by the continuity relation  $\nabla \cdot \sigma + b = 0$  where  $b$  represents body forces and  $\sigma \propto \mathbf{C} : \nabla \mathbf{u}$ . With some constraints, the solution would require  $u$  to be twice differential at all points in the domain and would be difficult to do analytically and computationally. It is therefore preferential to discretise the problem, and this is done by the finite element approach. The weak form equations are found by integrating the strong form differential equation and multiplying by some test/weight function  $w$  [3]. From the integration of the weak form the set of equations (in 1D for simplicity) is given as

$$\int \frac{dw}{dx} AE \frac{du}{dx} dx = \underbrace{\int w A \bar{t}}_{\text{Surface/Traction Forces}} + \underbrace{\int w b dx}_{\text{Body Forces}}, \quad (1)$$

where  $A$  is taken to be surface area. This form only constrains  $u$  to be piece-wise differentiable, simplifying the problem [4]. The aim is to discretise the domain by approximating  $u$ , typically by some polynomial. This is often done by using shape functions  $N(x)$  to interpolate the displacement field between the discretised points that make up individual elements. These shape functions are usually taken to be some polynomial which is determined such that the condition  $N_i(x_j) = \delta_{ij}$  [3], i.e. the shape function of node  $i$  is equal to unity at the node of the corresponding index and zero at the other nodal position's. The shape functions discretise the displacement field by

the relation [4]:

$$u \approx \sum_{i=1}^n N_i(x) d_i, \quad (2)$$

where  $n$  are the number of elemental nodes and  $d_i$  are unknown coefficients named nodal degrees of freedom. Generally the shape functions and nodal degrees of freedom are written in matrix notation, such that the generalised solution  $u = \mathbf{N}(\mathbf{x})\mathbf{d}$ . For ease, the Galerkin approximation is used to assume that the weight functions will have the same form as the displacement field, i.e discretised by the same shape functions ( $w(x) = \mathbf{N}(\mathbf{x})\mathbf{w}$ ) [4].

The integral expressions boil down to a relation analogous to that of Hooke's law with:

$$\mathbf{w}^T \int \frac{d\mathbf{N}^T}{dx} AE \frac{d\mathbf{N}}{dx} dx \mathbf{d} = \mathbf{w}^T \mathbf{N}^T A \bar{t} + \int \mathbf{w}^T \mathbf{N}^T b dx, \quad (3)$$

$$\mathbf{K}^e \mathbf{d}^e = \mathbf{f}^e, \quad (4)$$

where  $\mathbf{K}^e$  is the elemental stiffness matrix,  $\mathbf{d}^e$  is the elemental nodal degrees of freedom (DOFs) matrix (i.e nodal displacements), and  $\mathbf{f}^e$  is the elemental external force matrix.

In this paper, structural analysis is performed using the finite element method (FEM) within the limit of linear elasticity is displayed in Fig.1. The problem is a C-shape centroid that has two fixed ends at the  $x_1$  axis and a constant external load upon the uppermost edge with traction profile  $\bar{t} = 150 \text{ Nm}^{-1}$ .

Isoparametric finite elements are used to deduce the deformation of the solid object and the stresses and strains that vary throughout the solid. These results are evaluated for increasing finite elements (i.e. higher resolution).

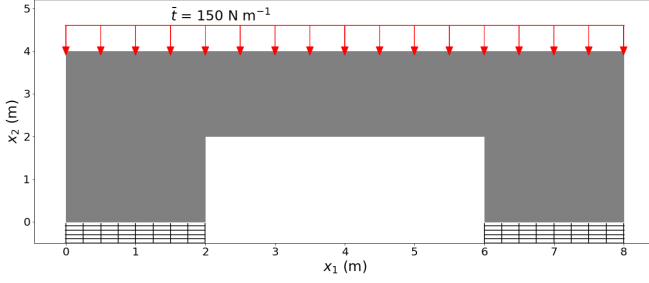


FIG. 1: Geometry of the solid mechanics finite element problem discussed in this paper. The grey sections represent solid material, and the cross-hatched black sections represent fixed boundary regions. A traction force is applied across the entirety of the top edge with a force profile of  $150 \text{ Nm}^{-1}$ , applied across the entire  $x_1$  domain.

## II. THEORY

### A. Linear Elasticity

In this paper, the problem considered is assumed to deform per the laws of linear elasticity, such that the solid will become internally stressed due to loading conditions. Fundamentally, the linear elastic model assumes infinitesimal strains ( $\epsilon_{ij}$ ), where second-order terms are assumed to be negligible, shown below:

$$E_{ij} = \frac{1}{2} \left( \frac{\partial u_i}{\partial X_j} + \frac{\partial u_j}{\partial X_i} + \frac{\partial u_i}{\partial X_j} \frac{\partial u_j}{\partial X_i} \right)^0 \rightarrow \epsilon_{ij}, \quad (5)$$

where  $\mathbf{u}$  is the displacement field taken to be the difference of the current position ( $\mathbf{x}$ ) to the starting/reference position ( $\mathbf{X}$ ). A constitutive relation is required to relate the components of strain and stress ( $\sigma_{ij}$ ). In this paper, thermal effects are neglected so the rate of change of internal energy ( $W$ ) of the system can be defined as [5],

$$\dot{W} = \frac{\partial W}{\partial \epsilon} : \frac{\partial \epsilon}{\partial t} = \sigma : \dot{\epsilon}. \quad (6)$$

The internal energy is often given as  $W = \frac{1}{2} \epsilon : \mathbf{C} : \epsilon$ , from which the constitutive relation can be found to be:

$$\sigma = \mathbf{C} : \epsilon \quad \text{or} \quad \sigma_{ij} = C_{ijkl} \epsilon_{kl}. \quad (7)$$

where for the 2D problem given in this paper the indices are either taken to be 1 or 2. Here,  $\mathbf{C}$  is the linear elasticity tensor (Rank 4) which relates the components of stresses to strains where there is 4 components of stress and strain. This system can be simplified given that  $W$  is scalar and such that  $W = \frac{1}{2} \epsilon : \mathbf{C} : \epsilon = \epsilon^T : \mathbf{C}^T : \epsilon^T = \epsilon : \mathbf{C}^T : \epsilon \rightarrow \mathbf{C}^T = \mathbf{C}$ , which means  $\mathbf{C}$  is constrained to be symmetric, therefore suggesting there is only 3 unique components of stresses and strains. This is often shown using the Voigt notation, which is formulated below for a 2D solid problem:

$$\begin{bmatrix} \sigma_{11} \\ \sigma_{22} \\ \sigma_{12} \end{bmatrix} = \begin{bmatrix} C_{1111} & C_{1122} & C_{1112} \\ C_{2211} & C_{2222} & C_{2212} \\ C_{1121} & C_{1222} & C_{1212} \end{bmatrix} \begin{bmatrix} \epsilon_{11} \\ \epsilon_{22} \\ 2\gamma_{12} \end{bmatrix}. \quad (8)$$

The element values of  $\mathbf{C}$  are constant and depend on the material properties of the solid, such as Young's modulus ( $E$ ) and the Poisson's ratio ( $\nu$ ). The form of the linear elasticity matrix is also dependent on the type of linear elastic problem you are considering. The length scales for the solid that is being modelled (Fig. 1) are (8 m, 4 m, 5 m) in the ( $x_1$ ,  $x_2$ ,  $x_3$ ) directions. With these length scales, it is sensible to use plane strain conditions rather than plane stress, typically used for thin plates/membranes. The plane stress condition assumes that there is no strain in the  $x_3$  direction (hence the decision only to consider 2D strains and stresses), simplifying  $\mathbf{C}$  to [5]:

$$[C] = \frac{E}{(1+\nu)(1-2\nu)} \begin{bmatrix} 1-\nu & \nu & 0 \\ \nu & 1-\nu & 0 \\ 0 & 0 & \frac{1}{2}(1-2\nu) \end{bmatrix} \quad (9)$$

where in this paper the values for  $E$  and  $\nu$  are taken to be 75 GPa and 0.32 respectively.

### B. Finite Element Method

The finite element method discussed briefly in the introduction (Sec.I) comes down to three fundamental relations, the relations between external force and stress, the constitutive relation between stress and strain (Sec.II A) and finally, the relation between strains and displacement. The domain for which the problem is considered is discretised into  $n$  nodal points, which make up  $n - 1$  quadrilateral elements with an elemental stiffness and force vector. To solve for the displacements in Eqn. 4 a global force vector and stiffness matrix needs to be augmented from the individual elemental forces and stiffnesses. The global force matrix will have a shape  $[n \times n_D, 1]$ , where  $n_D$  are the number of dimensions (i.e. components of force on each node), this is also the shape the displacement matrix will take. By inspection this leads to the global stiffness to be a square matrix of shape  $[n \times n_D, n \times n_D]$ , which is assembled from the elemental stiffness matrices, which for quadrilateral elements have shape  $[4 \times n_D, 4 \times n_D]$ .

### C. 2D - Isoparametric formalism

In this paper, the isoparametric formalisms are used to calculate the stresses and strains on the solid system shown in Fig. 1. Normalised (natural) coordinates systems must be used for isoparametric elements and are

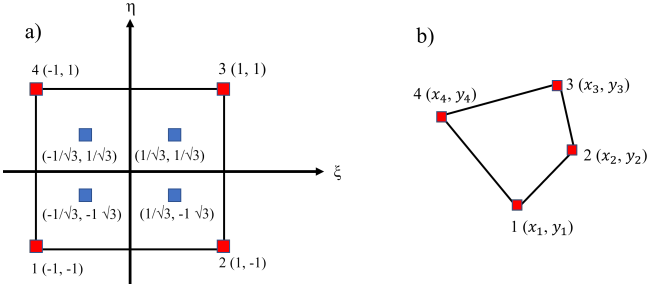


FIG. 2: Mapping between the natural coordinate system (a), and physical element domain (b). The red squares correspond to nodal points, with the blue squares representing the integration points used for performing numerical integration via Gaussian quadrature.

expressed in 2D as by the coordinates  $(\xi, \eta)$ , and therefore shape functions are defined in terms of these natural coordinates. The coordinate system for a typical quadrilateral element is shown in Fig. 2.

For quadrilateral elements, there are eight degrees of freedom per element (four nodes and two dimensions) thus nodal displacement vector of an element ( $d^e$ ) has eight components of the form:

$$[d_{1(1)}^e \ d_{2(1)}^e \ d_{1(2)}^e \ d_{2(2)}^e \ d_{1(3)}^e \ d_{2(3)}^e \ d_{1(4)}^e \ d_{2(4)}^e]^T \quad (10)$$

where the first subscript index denotes the degree of freedom, whilst the second denotes the node number within the element. Similarly to 1D one can interpolate the element displacements using shape functions such that  $\mathbf{u}^e(\xi, \eta) = \mathbf{N}^e(\xi, \eta)\mathbf{d}^e$ . As the coordinate system has been defined in natural coordinates  $(\xi, \eta)$ , it is favourable to define the shape functions in such a coordinate system. In the isoparametric formulation, the geometry of the element can also be described by the same set of shape functions and the nodal coordinates  $(\mathbf{c}^e)$ , in the physical coordinate frame, such that  $\mathbf{x}^e(\xi, \eta) = \mathbf{N}^e(\xi, \eta)\mathbf{c}^e$ . Note, the vector  $\mathbf{c}^e$  takes a similar form to  $\mathbf{d}^e$  as shown in Eqn. 10.

In order to satisfy these relations, the matrix of shape functions for a four-node element takes the following form:

$$\mathbf{N}^e = \begin{bmatrix} N_1^e & 0 & N_2^e & 0 & N_3^e & 0 & N_4^e & 0 \\ 0 & N_1^e & 0 & N_2^e & 0 & N_3^e & 0 & N_4^e \end{bmatrix} \quad (11)$$

These shape functions must once again obey the rule  $N_i(\xi_j) = \delta_{ij}$ , from which a polynomial solution can be found. This paper uses linear polynomial shape functions to interpolate between the four nodal points that construct each quadrilateral element. These shape functions are compactly formulated as follows [6]:

$$N_i^e(\xi, \eta) = \frac{1}{4} (1 + \xi_i \xi) (1 + \eta_i \eta) \quad (12)$$

where  $(\xi_i, \eta_i)$  represent the coordinates for the  $i^{th}$  node within the element, for which  $\xi$  and  $\eta$  are shown to satisfy  $-1 \leq \xi, \eta \leq 1$  in Fig. 2 (a).

The following subsections lay out the mathematical foundation for solving the global finite element problem  $\mathbf{K}\mathbf{D} = \mathbf{F}$ , for a solid comprised of many quadrilateral elements.

### 1. Global System

So far, only singular element formulations have been discussed when what is required is a formulation for the global system of multiple finite elements. In general, the extension from one element too many is relatively simple by employing the use of a set of Boolean matrices called gather matrices,  $\mathbf{L}^e$ . The definition of these gather matrices are such that the nodal displacements of each element can be taken from the global displacement matrix ( $\mathbf{D}$ )

The global stiffness matrix is found by gathering the information of the individual elemental stresses into a singular matrix by using Boolean matrices. These matrices gather the nodal displacements of each element from the global matrix i.e  $\mathbf{d}^e = \mathbf{L}^e \mathbf{D}$  [2].

This can be extended to reformulate the singular element formula  $\mathbf{K}^e \mathbf{d}^e = \mathbf{f}^e$  to a global formalism for  $n_e$  elements:

$$\mathbf{F} = \sum_{e=1}^{n_e} \mathbf{L}^{eT} \mathbf{f}^e = \sum_{e=1}^{n_e} \mathbf{L}^{eT} \mathbf{K}^e \mathbf{d}^e = \sum_{e=1}^{n_e} \mathbf{L}^{eT} \mathbf{K}^e \mathbf{L}^e \mathbf{D}. \quad (13)$$

From inspection, the assembled system matrix (global stiffness) is given by [5]:

$$\mathbf{K} = \sum_{e=1}^{n_e} \mathbf{L}^{eT} \mathbf{K}^e \mathbf{L}^e. \quad (14)$$

Thus, to formulate the global system equation, the formalism's for elemental stiffness and external force is required. The next couple of subsections goes over how these are calculated.

### 2. Stiffness Matrix - $\mathbf{K}^e$

Analogous to the definition for the elemental stiffness shown in Eqn 3, the elemental stiffness for 2D elements are found by evaluating the following integral

$$\mathbf{k}^e = \int_{\Omega_e} \mathbf{B}^{e,T} \mathbf{C} \mathbf{B}^e \Omega = t_{x_3} \int \mathbf{B}^{e,T} \mathbf{C} \mathbf{B}^e d\mathbf{x}, \quad (15)$$

where  $\mathbf{B}$  is the strain-displacement matrix,  $\mathbf{C}$  is the linear elasticity matrix discussed in Sec. II A and  $t_{x_3}$  is the out-of-plane thickness. The strain-displacement matrix is

related to the derivatives of the shape functions, (again analogous to Eqn 3), and it is defined as a  $[3, 8]$  matrix as follows:

$$\mathbf{B}^e = \nabla_{\mathbf{s}} \mathbf{N}^e, \quad (16)$$

where:

$$\nabla_{\mathbf{s}} = \begin{bmatrix} \frac{\partial}{\partial x_1} & 0 \\ 0 & \frac{\partial}{\partial x_2} \\ \frac{\partial}{\partial x_2} & \frac{\partial}{\partial x_1} \end{bmatrix}, \quad (17)$$

giving:

$$\begin{bmatrix} \frac{\partial N_1^e}{\partial x_1} & 0 & \frac{\partial N_2^e}{\partial x_1} & 0 & \frac{\partial N_3^e}{\partial x_1} & 0 & \frac{\partial N_4^e}{\partial x_1} & 0 \\ 0 & \frac{\partial N_1^e}{\partial x_1} & 0 & \frac{\partial N_2^e}{\partial x_1} & 0 & \frac{\partial N_3^e}{\partial x_1} & 0 & \frac{\partial N_4^e}{\partial x_1} \\ \frac{\partial N_1^e}{\partial x_2} & \frac{\partial N_1^e}{\partial x_1} & \frac{\partial N_2^e}{\partial x_2} & \frac{\partial N_2^e}{\partial x_1} & \frac{\partial N_3^e}{\partial x_2} & \frac{\partial N_3^e}{\partial x_1} & \frac{\partial N_4^e}{\partial x_2} & \frac{\partial N_4^e}{\partial x_1} \end{bmatrix}. \quad (18)$$

So far, the stiffness matrix is represented in terms of physical coordinates and needs to be redefined in terms of natural coordinates to incorporate our shape function basis described in the previous section (Eqn.12).

The integral displayed in Eqn. 15 can be altered by defining the transformation Jacobian ( $\mathbf{J}^e$ ) :

$$\mathbf{J}^e = \frac{\partial \mathbf{x}^e}{\partial \xi} = \frac{\partial \mathbf{N}^e}{\partial \xi} \mathbf{c}^e, \quad (19)$$

in matrix notation:

$$\mathbf{J}^e = \begin{bmatrix} \frac{\partial N_1^e}{\partial \xi} & \frac{\partial N_2^e}{\partial \xi} & \frac{\partial N_3^e}{\partial \xi} & \frac{\partial N_4^e}{\partial \xi} \\ \frac{\partial N_1^e}{\partial \eta} & \frac{\partial N_2^e}{\partial \eta} & \frac{\partial N_3^e}{\partial \eta} & \frac{\partial N_4^e}{\partial \eta} \end{bmatrix} \begin{bmatrix} c_{1(1)}^e & c_{2(1)}^e \\ c_{1(2)}^e & c_{2(2)}^e \\ c_{1(3)}^e & c_{2(3)}^e \\ c_{1(4)}^e & c_{2(4)}^e \end{bmatrix}, \quad (20)$$

where the natural derivatives of the shape functions can be readily found from Eqn 12 giving:

$$\frac{\partial \mathbf{N}^e}{\partial \xi} = \frac{1}{4} \begin{bmatrix} \eta - 1 & 1 - \eta & 1 + \eta & -\eta - 1 \\ \xi - 1 & 1 - \xi & 1 + \xi & 1 - \xi \end{bmatrix}. \quad (21)$$

The Jacobian helps reformulate both the transformation of the strain-displacement matrix and the infinitesimal  $d\mathbf{x}$ , such that:

$$\mathbf{B}^e = \frac{\partial \xi}{\partial \mathbf{x}^e} \frac{\partial \mathbf{N}^e}{\partial \xi} = (\mathbf{J}^e)^{-1} \frac{\partial \mathbf{N}^e}{\partial \xi}, \quad (22)$$

$$d\mathbf{x} = d\mathbf{x}_1 d\mathbf{x}_2 = \det \mathbf{J}^e d\xi d\eta. \quad (23)$$

This transforms elemental stiffness matrix to be defined in terms of the natural coordinate set,

$$\mathbf{k}^e = t_{x_3} \int_{-1}^1 \int_{-1}^1 \mathbf{B}^{e,T}(\xi, \eta) \mathbf{C} \mathbf{B}^e(\xi, \eta) \det \mathbf{J}^e d\xi d\eta. \quad (24)$$

Such an integral is typically solved numerically, which is done in this paper using Gaussian quadrature. The Gauss quadrature formulation of Eqn. 25 is given by:

$$t_{x_3} \sum_{i=1}^{n_\xi=2} \sum_{j=1}^{n_\eta=2} w_i w_j \mathbf{B}^{e,T}(\xi_i, \eta_i) \mathbf{C} \mathbf{B}^e(\xi_i, \eta_i) \det \mathbf{J}^e(\xi_i, \eta_i), \quad (25)$$

for four integration points (Fig. 2 (a)), where  $\xi_1 = -\frac{1}{\sqrt{3}}$ ,  $\xi_2 = \frac{1}{\sqrt{3}}$ ,  $\eta_1 = -\frac{1}{\sqrt{3}}$ ,  $\eta_2 = \frac{1}{\sqrt{3}}$ , with the weight functions  $w_i$  and  $w_j$  being equal to unity.

### 3. Force Matrix - $\mathbf{F}^e$

For the particular problem that is modelled in this paper, there is only one source of external force that is applied to the solid. This is displayed in Fig. 1, by the force profile along the top edge of the solid system with a magnitude taken to be  $|\bar{\mathbf{t}}| = 150 \text{ Nm}^{-1}$  pointing in the negative  $x_2$  direction. The net force can thus be determined by an integral which spans over the domain in which  $\bar{\mathbf{t}}$  acts:

$$\mathbf{F} = \int_0^{L_{x_1}=8} -150 dx_1 \mathbf{e}_{\mathbf{x}_2} = -1200 \mathbf{e}_{\mathbf{x}_2} \text{ N}. \quad (26)$$

The above integral, of course, needs to be discretised, similar to the RHS of Eqn. 3 however, this above condition is helpful to check that the forces in the  $x_1$  direction and  $x_2$  are found to be 0 and -1200 N, respectively, when the global force matrix is initialised.

Discretising the integral, the nodal force vectors for each element can be deduced from [5]:

$$f_e = \int_{l+l_e}^{l+2l_e} \mathbf{N}^{e,T} \bar{\mathbf{t}} dx_1, \quad (27)$$

Where  $l$  is some arbitrary point in the domain, and  $l_e$  is the length of the quadrilateral element in the  $x_1$  direction (i.e. the width). Given that the shape functions are defined in the natural coordinate space, solving this integral in the natural coordinate space is beneficial. From the geometry of the problem, the force profile only acts along the edge between nodes 3 and 4 in the natural coordinate system (shown in Fig. 2). This edge in physical space corresponds to  $\eta = 1$  in natural coordinates and simplifies the shape function matrix to only be dependent on the shape functions corresponding to nodes 3 and 4. Converting from real to natural coordinates where  $l + l_e \leq x_1 \leq l + 2l_e$ ;  $-1 \leq \xi \leq 1$ , it is found that:

$$x_1 = \frac{1}{2}(2l + 3l_e) = \frac{l_e}{2} \xi \rightarrow dx_1 = \frac{l_e}{2} d\xi. \quad (28)$$

Using all of this information, the integral can now be solved in natural coordinate space to give the elemental nodal force vector  $\mathbf{f}^e$ :

$$\begin{aligned}
f_e &= \frac{l_e}{2} \int_{-1}^1 \frac{1}{2} \begin{bmatrix} 0 & 0 \\ 0 & 0 \\ 0 & 0 \\ 1+\xi & 0 \\ 0 & 1+\xi \\ 1-\xi & 0 \\ 0 & 1-\xi \end{bmatrix} \begin{bmatrix} 0 \\ -150 \end{bmatrix} d\xi \\
&= \frac{l_e}{2} \begin{bmatrix} 0 & 0 \\ 0 & 0 \\ 0 & 0 \\ 0 & 0 \\ 1 & 0 \\ 0 & 1 \\ 1 & 0 \\ 0 & 1 \end{bmatrix} \begin{bmatrix} 0 \\ -150 \end{bmatrix} = \frac{l_e}{2} \begin{bmatrix} 0 \\ 0 \\ 0 \\ 0 \\ 0 \\ -150 \\ 0 \\ -150 \end{bmatrix} \text{ N.}
\end{aligned} \tag{29}$$

The global force vector can then be found for the entire set of nodal points using the gather matrices discussed in Sec.II C 1 and shown mathematically in Eqn.13.

#### 4. Stresses and Strains - $\epsilon^e$ , $\sigma^e$

Once the global nodal displacements are attained by solving  $\mathbf{D} = \mathbf{K}^{-1}\mathbf{F}$ , it is necessary to produce nodal DOF matrices for each element ( $d^e = \mathbf{L}^e\mathbf{D}$ ) in order to evaluate the strains and stresses for the entire system.

Strains and stresses for each element are evaluated at each of the integration points  $I_p$  as  $\epsilon_{I_p}^e = \mathbf{B}_{I_p}^e \mathbf{d}^e$  and  $\sigma_{I_p}^e = \mathbf{C} \epsilon_{I_p}^e$  respectively [5].

The overall element strains and stresses are calculated in Voigt notation from Gaussian quadrature giving:

$$\epsilon^e = \begin{bmatrix} \epsilon_{11} \\ \epsilon_{22} \\ \gamma_{12} \end{bmatrix}^e = \sum_{I_p=1}^{n_p} \epsilon_{I_p}^e \det J_{I_p}^e w_{I_p} t_{x_3}, \tag{30}$$

$$\sigma^e = \begin{bmatrix} \sigma_{11} \\ \sigma_{22} \\ \sigma_{12} \end{bmatrix}^e = \sum_{I_p=1}^{n_p} \sigma_{I_p}^e \det J_{I_p}^e w_{I_p} t_{x_3}. \tag{31}$$

### III. IMPLEMENTATION AND ANALYSIS

The finite element approach described in the above sections is implemented into a computational model to calculate the elemental stresses, strains and nodal displacements for the problem geometry displayed in Fig. 1. All elements within the solid grey region were calculated to have a non zero stiffness using the formalism's laid out in Sec.II C 2, with elements and nodal points within the bounded empty region having set null elemental stiffness and nodal displacement. Boundary conditions were

also required to ensure that the nodal points at the fixed edges remained stationary, which is done by enforcing the nodal displacements at these boundaries to be null, i.e. displacements in either direction are set to zero at these nodes. The problem is split about the  $x_1 = 4$  line, where the nodal displacements perpendicular to the line of symmetry is taken to be zero. Due to the symmetry of the problem, the reaction from one side of the line of symmetry will ultimately cancel out the action from the other side (Newton's 3rd law). The stress, strains, and nodal displacements can only be found for one side and then reflected to represent the other half. To simplify the calculations, a reduced set of equation are found by constricting the linear algebra problem to solve for non-zero displacement nodal components (i.e ignore the boundary relevant terms in  $K$  and  $F$  and the known symmetry components discussed above). Calculations are performed for a range of element sizes (from  $2^3$  elements to  $2^{15}$  elements) to observe at what point the finite element mesh converges to the correct deformed mesh.

Convergence plots were found for both the maximum stresses and strains present within the deformed mesh, as it is expected that these converge to lower and lower values as the mesh size increases. The discretisation error for elemental stresses and strains for varying mesh size was estimated using the normalised error formula:  $\mathbf{a} \in \epsilon, \sigma$ ,

$$\|\bar{e}\|_{L_2} = \frac{\|\mathbf{a} - \mathbf{a}^{\text{ex}}\|_{L_2}}{\|\mathbf{a}^{\text{ex}}\|_{L_2}} = \left( \frac{\sum_{i=1}^n |a_i - a_i^{\text{ex}}|^2}{\sum_{i=1}^n |a_i^{\text{ex}}|^2} \right)^{\frac{1}{2}}, \tag{32}$$

where the exact result  $\mathbf{a}^{\text{ex}}$  was taken to be equivalent to the results of the largest mesh simulation ( $2^{15}$  elements), as it is assumed the FEM model has converged to the correct result at this point.

## IV. RESULTS AND DISCUSSION

### A. Nodal Displacement

The resulting nodal displacements for a variety of mesh sizes are displayed in Fig.3, for which the displacements are scaled by a factor of  $5 \times 10^7$  to help observe the relative displacement between nodes. From the observed deformed meshes in red, it can be seen that there is far more variation in the  $x_2$  direction, given that this is parallel to the applied loading force, and there is less observed deformation in the  $x_1$ .

The maximal displacement in the  $x_2$  direction is always located around the axis of symmetry  $x_1 = 4$ , which makes sense given that the material in the centre is furthest away from the fixed supporting solid beams, and the locality of the force is likely to be more heavily concentrated at this point due to symmetry. Given that the Poisson ratio of this material is positive, the expectation that the solid would expand out laterally was expected as the applied force aims to compress the solid vertically.

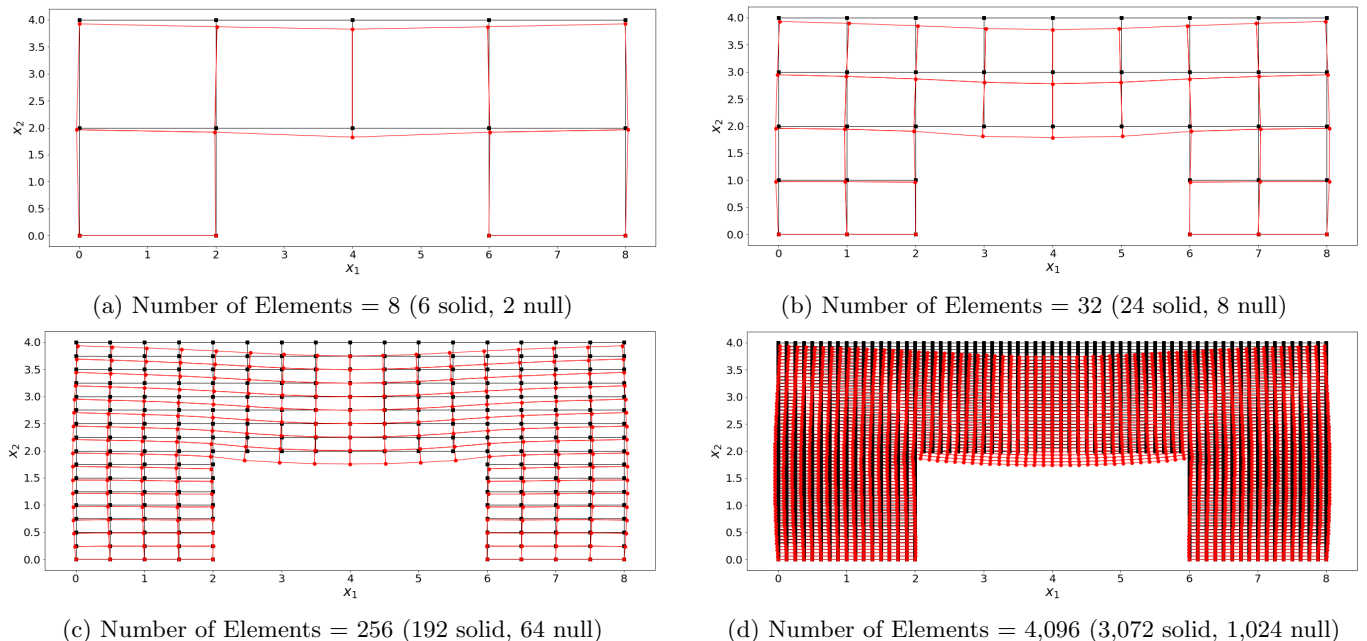


FIG. 3: Resulting nodal displacement from FEM solver using various mesh sizes. Deformed meshes (red) are scaled by a factor of  $5 \times 10^7$ . Convergence to the true deformation is observed by increasing the number of elements.

Displacements in the  $x_1$  direction are maximal around the centre of the edges  $x_1 = 0$  and  $x_1 = 8$ , and the upper-most edges where traction is applied (except the centre at which the  $x_1$  displacements are zero due to symmetry). This behaviour is more readily shown in Fig.4 which displays the displacement fields for the highest resolution grid simulate ( $2^{15}$  elements), which is taken to be the exact numerical result.

As the resolution of the grid increases, the nodal displacements are observed to converge to their actual value, with more accurate deformation structures being visualised for more refined meshes. The convergence is visualised in Figs.3 (a)-(d), where the increasing number of elements leads to a smoother deformation picture. Plotting the maximum nodal displacement in both the  $x_1$  and  $x_2$  for various resolutions elements shows the convergence of the finite element approach implemented.

The resolutions in the  $x_2$  and  $x_1$  are increased by a factor of two in alternating simulation runs. More significant changes in the recorded maximum displacement are found when the resolution is grown for the  $x_1$  axis until large amounts of elements are simulated (i.e. after the system has converged). This effect makes sense when considering how the traction force operates on the solid system. The traction field is dependent on the element length in the  $x_1$  axis; therefore, increasing the resolution in  $x_1$  distributes the applied traction among a more significant number of nodes, which is more physically accurate.

The maximum nodal displacement results show that for mesh sizes  $> 10^3$  elements, the nodal displacements are within a 4 % error of the actual numerical result,

and for mesh sizes greater than  $4 \times 10^3$  and  $8 \times 10^3$  elements, the results are within a 1 % and 0.5% error respectively. It would therefore suggest that if one was to only care about generating accurate nodal displacement results, using resolutions of  $> 8 \times 10^3$  are the most suitable to use. However, if one wants to compromise the accuracy to benefit from a shorter computation time, then using resolutions of  $> 1 \times 10^3$  elements produces an ideal balance. Note, the computational cost scales with complexity  $O((2n)^3)$ , as the global stiffness matrix must be inverted to find the displacements.

Going back to the discussion of linear elasticity in Sec. II A, small deformations are expected if our model is consistent with the assumptions of linear elasticity. The order of magnitude of the calculated displacements is on the nano-scale, with the length scale of the original system being of the order of metres. Thus, our results are consistent with the assumptions of linear elasticity, suggesting that if external forces were to be removed, the system would relax back into its original geometry.

## B. Strains and Stresses

The elemental stress and strain components are shown to decrease towards convergence as the resolution of the system increases, as shown in Fig.6. Increasing the resolution in the  $x_1$  and  $x_2$  decreases the recorded stresses and strains equivalently, unlike what was observed for displacements.

Fig.6 also show that for each resolution simulated, the stress component parallel to the  $x_2$  axis is most signifi-

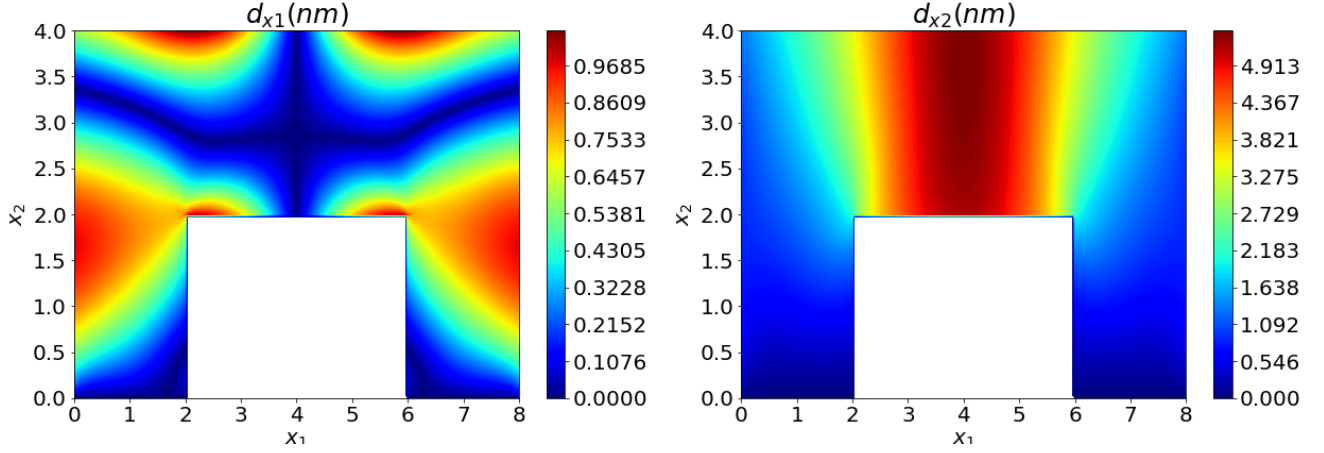


FIG. 4: Displacement field in both the  $x_1$  and  $x_2$  directions, attained from the highest resolution simulation (Number of elements =  $2^{15}$ ). Lateral displacements are observed to be maximal towards the edges of the solid, and vertical displacements are observed to be maximal at the axis of symmetry ( $x_1 = 4$ ).

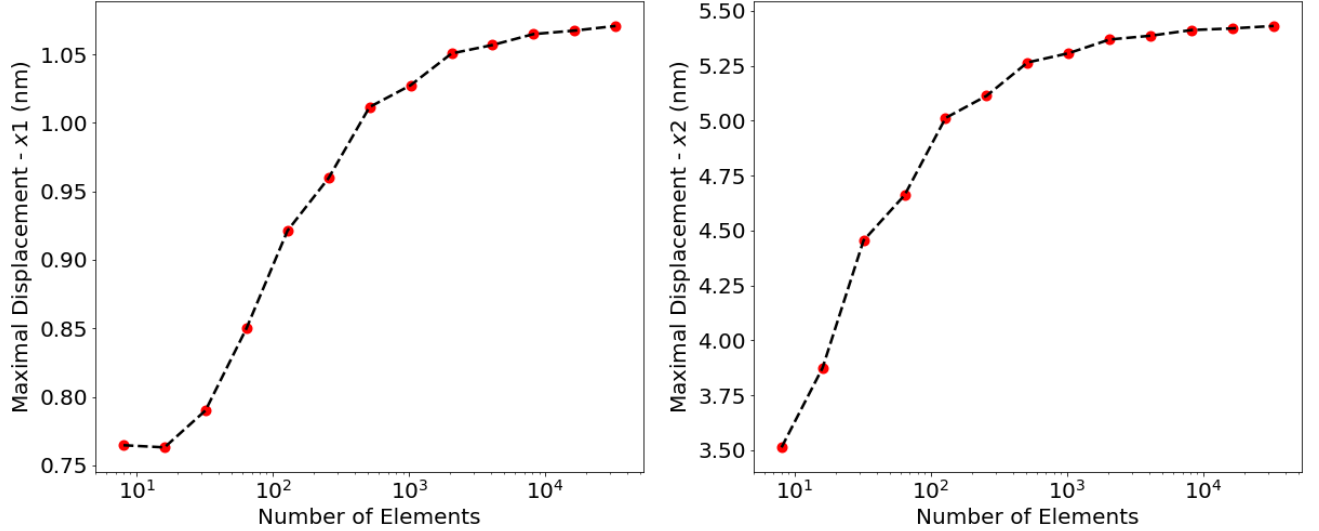


FIG. 5: Maximum nodal displacement in both the  $x_1$  and  $x_2$  observed as the resolution of the grid is increased. The FEM method implemented for this problem is observed to have converged for a mesh sizes  $> 10^3$  elements.

cant, which is expected given that the external force acts in the same direction. The strain components  $\epsilon_{22}$  and  $\gamma_{12}$  are found to be similar, which was an interesting result. It would be reasonable to expect the  $\epsilon_{22}$  components to be most significant given the nature of the applied load. However, given the lateral expansion of the solid and the vertical compression, it makes sense that the shear component is also comparable to the vertical strain component, given that the vertical displacement is more significant. To explore further how the stress/strain components vary throughout the solid, contour plots were made to find the stress/strain fields.

The spatial variability of the elemental strain and stress components are displayed in Fig.7, where the stress/strain for each element is assumed to be concentrated at the element centre. The contour plots show the magnitude of each component is maximal at the in-

side corners (coordinates (2, 2) and (6,2)). The variation in stress/strain components is shown in Figs.7 (a) (b), to be relatively minimal outside the inner corners, apart from the components in the 11 direction. The  $\epsilon_{11}$  is shown to be prominent at the uppermost edge due to the relatively high lateral displacement as shown in Fig. 4. Lateral elongation in the  $x_1$  is favourable for elements containing nodes at the centre of the upper edge due to the nodes at the axis of symmetry having to be remained fixed due to symmetry. The high-resolution contour (Fig. 7b) best shows the actual locality of the maximal stresses and strains in a deformed solid system. Once again, this showed that pretty much all the stress/strain is concentrated at the inner corners.

Discretisation errors for each resolution size were estimated using Eqn.32 to quantify the solution quality at each resolution. The results were then plotted as a



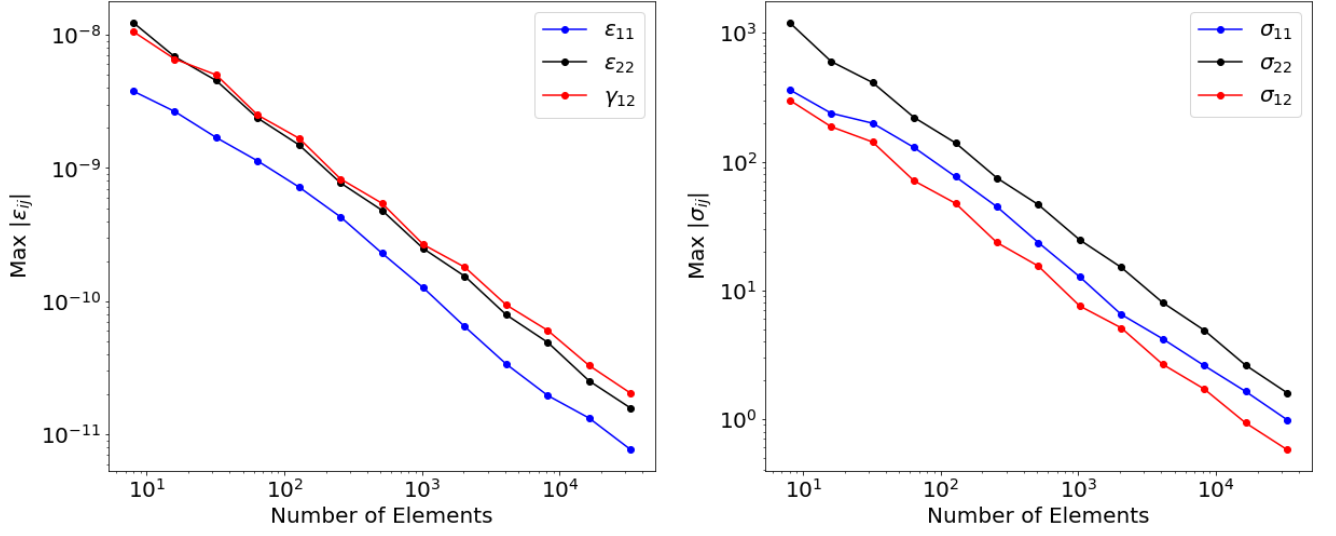
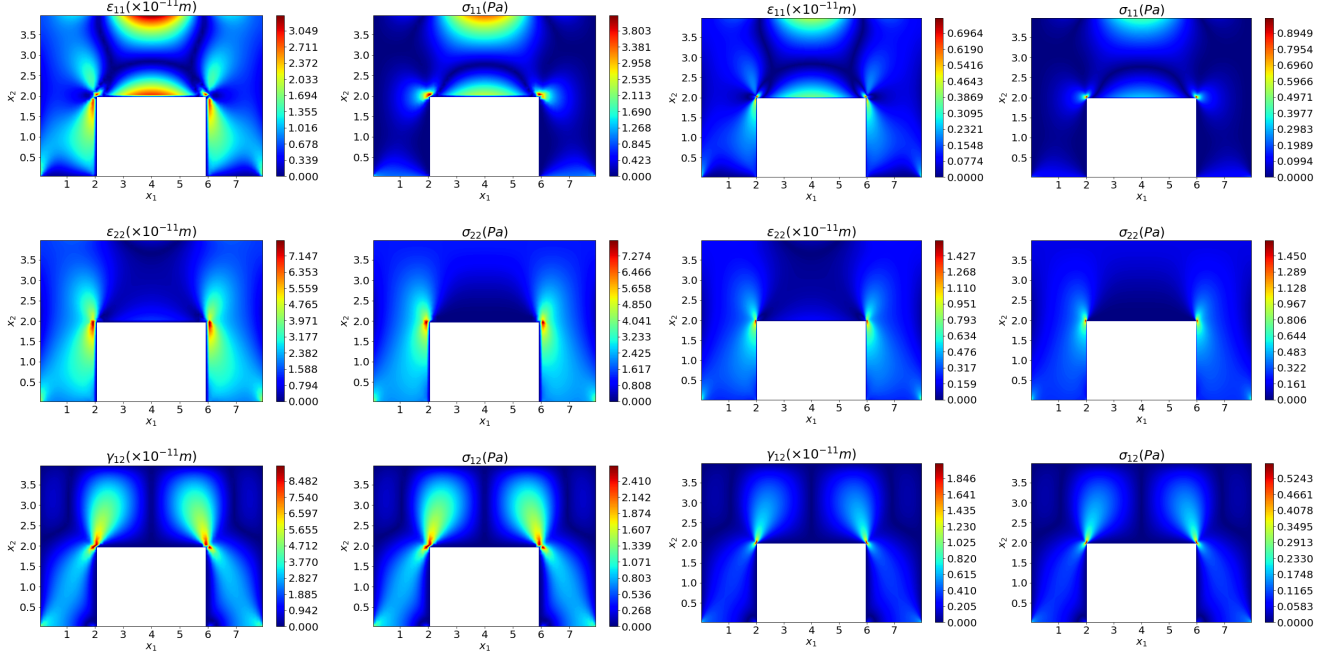


FIG. 6: Convergence of recorded stress and strain components which increasing resolution. Components dependent on the deformation in the  $x_2$  direction are shown to be largest given the nature of the applied force.



(a) Number of Elements = 4,096 (3,072 solid, 1,024 null)

(b) Number of elements = 32,768 (24,576 solid, 8,192 null)

FIG. 7: Contour maps display each component's elemental strain and stress fields throughout the deformed solid. Figure (a) shows the variation of the elements throughout the solid, and figure (b), with its far larger resolution, helps to display the exact locality of the peak stress and strains.

function of elemental area to try and observe if there was some polynomial relation between the resolution size and accuracy of the computational model. Bayesian ridge regression techniques were used with a polynomial basis to estimate a fit for the data. The elemental stress and strain for element one in each simulation size were used to compare each simulation in roughly the same region each time. The results are shown in Fig.8. The fit weights are

found from the posterior distribution of the Bayesian regression, where the error ( $\|\bar{e}\|_{L_2}$ ), is found to relate to the elemental area ( $A$ ) by:

$$\|\bar{e}(\epsilon)\|_{L_2} = 461A - 79A^2 + 13A^3 \quad \text{for Strain}, \quad (33)$$

$$\|\bar{e}(\sigma)\|_{L_2} = 396A - 29A^2 + 6A^3 \quad \text{for Stress}. \quad (34)$$

A degree 3 fitting polynomial modelled the data best (i.e.



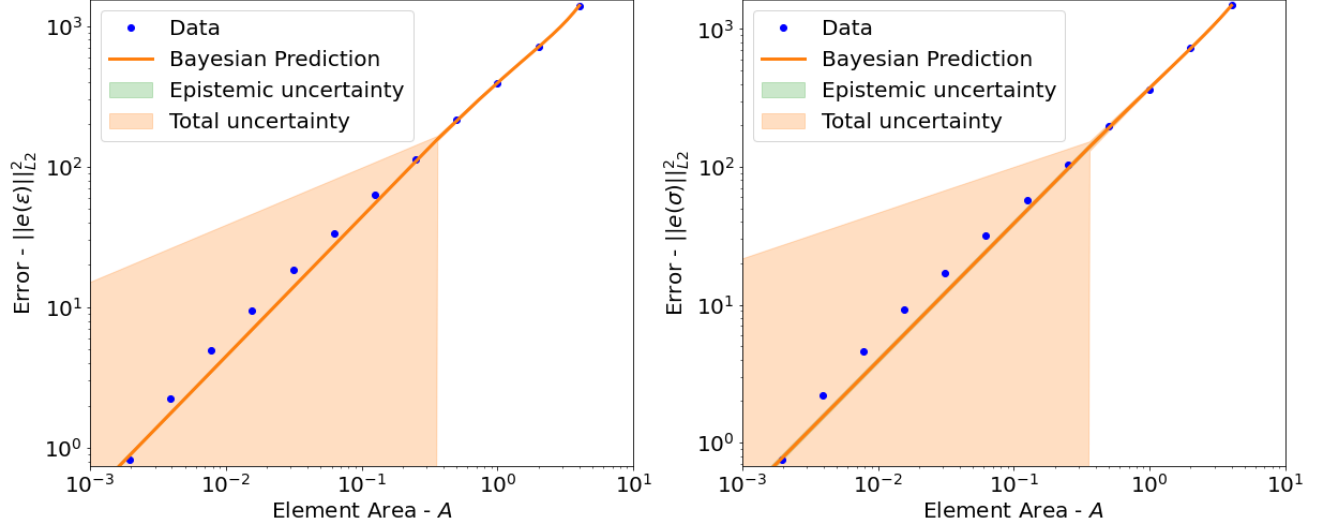


FIG. 8: Discretisation error for varying elemental areas (sizes), where the exact solution in which the errors are judged and normalised by is taken to be the highest resolution simulation ( $2^{15}$  elements). Bayesian ridge regression techniques were used using a polynomial basis set. The polynomial degree was chosen to be the degree that maximised the log of the likelihood distribution.

maximised the log of the likelihood), suggesting that using far smaller elemental sizes provides a much more accurate model. However, the exact nature of the relation between the error and elemental area needs to be taken with caution, as observed by the relatively large errors predicted from the Bayesian regression. The fit has very little uncertainty for more extensive areas and matches the data almost perfectly; however, as the elemental sizes become comparable to the reference solution, the error in the fit start to become increasingly more prominent with a fanning nature. Ultimately this suggests that it would be best to use a reference solution taken to be far more significant than the one taken in this paper (e.g. 200,000-400,000 elements rather than 30,000). Hopefully, this would mean that the area values for the data points are so close to the reference solution that these significant errors occur, like which is observed for the four largest area data points in Fig 8.

However, for the reference solution used, the error was observed to decrease dramatically with an increased resolution which shows that the computational model was working as expected and therefore could be seen to be taken reliable results, which was all that is necessary for this paper. The error take a similar form for both the stresses and strains, with both empirical relations given by Eqns.33 & 34 having similar amplitudes for each polynomial coefficient.

### C. Reaction Force

Reaction forces should arise at the fixed boundary edges. Using the found nodal displacements, the whole system of linear equations can be solved rather than the

reduced non-zero displacement equations, producing the full force matrix containing the reactive forces at the fixed boundaries. Components in the  $x_1$  and  $x_2$  direction are summed to resolve the net force at the boundary, with the results displayed in Fig.9. The results are only for the fixed left-hand edge as the right-hand edge has an equal and opposite reaction (i.e. same magnitudes but the opposite direction ( $\theta$ )). Fig.9 shows that the net reaction force is heavily dominated by its  $x_2$  component, which is counteracting the external force applied at the uppermost edge (hence why it is flat at 600 N, half of the -1200 N force applied by the external load across the entire domain). The dominance of the  $x_2$  reaction component is also seen by the relatively large angle of  $77^\circ$  to the  $x_1$  axis. However, the variation of the reaction throughout various grid resolutions is solely dependent on the  $x_1$  component, which is less constricted by an applied external load. The convergence of the maximal components of reaction force observed for the set of nodes on the fixed boundary edges is shown in Fig.10. The  $x_1$  and  $x_2$  component behaviour is very different. The  $x_2$  component is observed to have a descending step nature, where the sharp vertical drops correspond to solutions where grid resolution has increased in the  $x_1$  axis rather than  $x_2$ . This is due to the applied force being dependent on the resolution in the  $x_1$  axis as discussed in Sec.II C 3. The  $x_1$  component oscillates for the low-resolution simulations, which is damped as the resolution increases, and convergence is observed. Ultimately, these results further prove that the finite element analysis converges towards the correct structural deformation as the resolution is increased, especially for  $10^3$  elements.

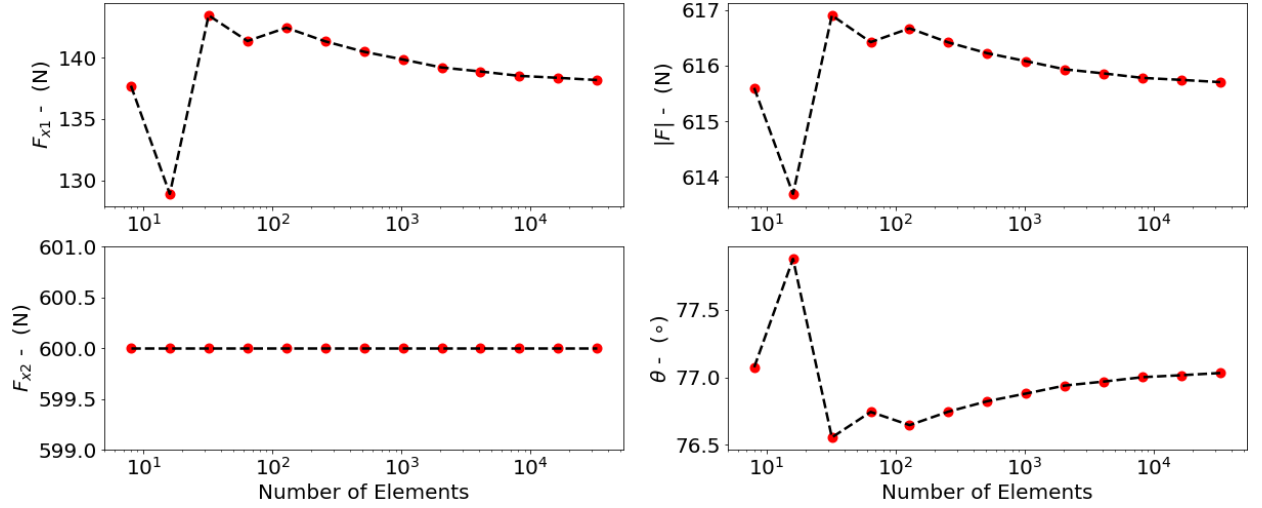


FIG. 9: Reaction force data at the fixed edge on the left hand side of the axis of symmetry (i.e edge (0,0) to (2,0)). The result on the right hand side was found to produce an equal and opposite force (i.e. equal magnitude, opposite direction ( $\theta$ )).

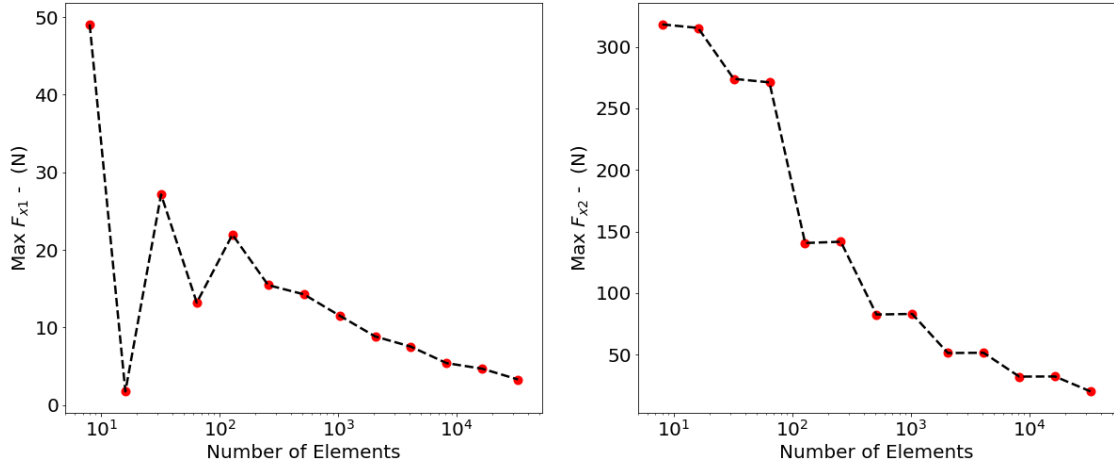


FIG. 10: Convergence of the maximal components of reaction force observed for the set of nodes on the fixed boundary edges. The  $x_2$  component is observed to have a descending step profile, where the sharp vertical drops correspond to solutions where grid resolution has increased in the  $x_1$  axis rather than  $x_2$ .

## V. CONCLUSIONS

Structural analysis was performed using isoparametric finite element analysis for a range of resolutions. Inspection of the nodal displacements found that for system sizes  $> 10^3$  elements were close to or had reached convergence with the maximum achieved nodal displacement in the  $x_1$  and  $x_2$  displacement being around 1.05 nm and 5.50 nm, respectively. Given the size of these found displacements to the scale of the problem geometry, the results were consistent with the theory of linear elasticity.

The general deformation picture showed that the material bends downwards in the centre region of the C-shape where there is no solid underneath to carry any burden of the applied load, with lateral movement outwards being observed due to the material's positive Poisson's ratio.

Analysis of the elemental stresses and strains showed

that the elemental stress and strain were observed to decrease with increasing resolution towards convergence for every component. The stresses and strains were predominantly concentrated at the vertices (2,2) and (6,2) for all three components, with the best stress-strain fields being observed for higher resolution results.

Discretisation errors for the calculated elemental stress and strain were judged to have a cubic polynomial relation; however, using a more extensive reference solution would improve the fit to produce a more accurate model.

To build upon the work done in this paper, using higher-order shape functions and element schemes would significantly improve the model's accuracy. One such way is to use quadrilateral elements with additional mid-side nodes ('quadratic' elements), which requires a set of new shape functions as discussed in Ref.[6].

- 
- [1] K. Bathe, *Finite Element Procedures* (Cambridge, 2006).
  - [2] O. Zienkiewicz, R. Taylor, and J. Zhu, *The Finite Element Method: Its Basis and Fundamentals* (Butterworth-Heinemann, 2013).
  - [3] I. Babuška, U. Banerjee, and J. Osborn, Generalized finite element methods: Main ideas, results, and perspective, *International Journal of Computational Methods* **1**, 67 (2004).
  - [4] A. Ern and J. Guermond, *Theory and practice of finite elements* (Springer, 2004).
  - [5] J. Fish and T. Belytschko, *A First Course in Finite Elements* (John Wiley Sons, Ltd, 2007).
  - [6] I. Ergatoudis, B. Irons, and O. Zienkiewicz, Curved, isoparametric, “quadrilateral” elements for finite element analysis, *International Journal of Solids and Structures* **4**, 31 (1968).